

VIP Photo-Initiated Cobalt-Catalyzed Radical Olefin Hydrogenation

Special Issue

Sier Sang,^[a] Tobias Unruh,^[b] Serhiy Demeshko,^[a] Luis I. Domenianni,^[b] Nicolaas P. van Leest,^[c] Philipp Marquetand,^[d] Felix Schneck,^[a] Christian Würtele,^[a] Felix J. de Zwart,^[c] Bas de Bruin,^[c] Leticia González,^[d] Peter Vöhringer,^[b] and Sven Schneider*^[a]

Abstract: Outer-sphere radical hydrogenation of olefins proceeds via stepwise hydrogen atom transfer (HAT) from transition metal hydride species to the substrate. Typical catalysts exhibit M–H bonds that are either too weak to efficiently activate H₂ or too strong to reduce unactivated olefins. This contribution evaluates an alternative approach,

that starts from a square-planar cobalt(II) hydride complex. Photoactivation results in Co–H bond homolysis. The three-coordinate cobalt(I) photoproduct binds H₂ to give a dihydrogen complex, which is a strong hydrogen atom donor, enabling the stepwise hydrogenation of both styrenes and unactivated aliphatic olefins with H₂ via HAT.

Introduction

Homogeneous olefin hydrogenation is a mature and versatile synthetic methodology.^[1] Many catalysts follow mechanisms defined by H₂ oxidative addition, olefin insertion, and alkane reductive elimination or, alternatively, redox neutral routes via hydrogenolysis of the hydrocarbyl complex intermediates. In recent years, the sustainability of olefin hydrogenation protocols was considerably advanced by the development of many first-row transition metal pre-catalysts,^[2] including several cobalt precursors (Figure 1).^[3] Experimental and computational studies identified cobalt hydrocarbyl key intermediates within olefin insertion-based mechanisms.^[4] The current renaissance of

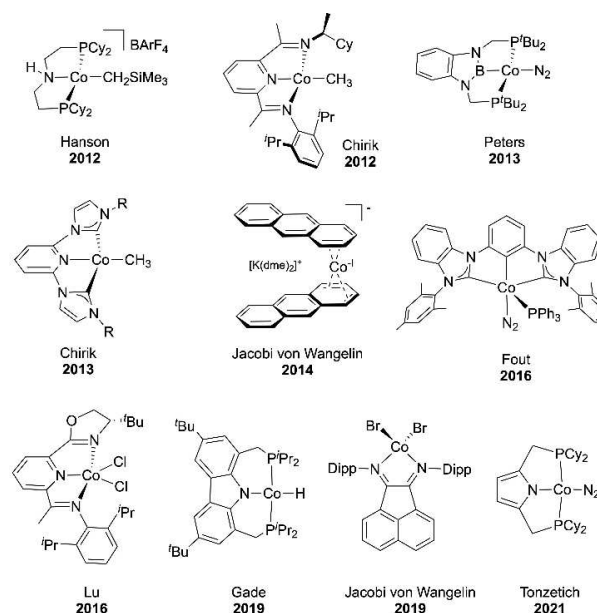


Figure 1. Molecular cobalt catalyst precursors for olefin hydrogenation.

[a] S. Sang, Dr. S. Demeshko, Dr. F. Schneck, Dr. C. Würtele, Prof. Dr. S. Schneider
Universität Göttingen
Institut für Anorganische Chemie
Tammannstraße 4, 37077 Göttingen (Germany)
E-mail: sven.schneider@chemie.uni-goettingen.de

[b] T. Unruh, Dr. L. I. Domenianni, Prof. Dr. P. Vöhringer
Institut für Physikalische und Theoretische Chemie
Rheinische Friedrich-Wilhelms-Universität
Wegelerstrasse 12, 53117 Bonn (Germany)

[c] N. P. van Leest, F. J. de Zwart, Prof. Dr. B. de Bruin
Van't Hoff Institute for Molecular Sciences
University of Amsterdam
Science Park 904, 1098 XH Amsterdam (The Netherlands)

[d] Dr. P. Marquetand, Prof. Dr. Dr. h.c. L. González
Institute of Theoretical Chemistry, Faculty of Chemistry
University of Vienna
Währinger Straße 17, 1090 Vienna (Austria)

Supporting information for this article is available on the WWW under <https://doi.org/10.1002/chem.202101705>

Part of a Special Issue on Contemporary Challenges in Catalysis.

© 2021 The Authors. Chemistry - A European Journal published by Wiley-VCH GmbH. This is an open access article under the terms of the Creative Commons Attribution Non-Commercial License, which permits use, distribution and reproduction in any medium, provided the original work is properly cited and is not used for commercial purposes.

organic radical chemistry^[5] also revived interest in an alternative mechanistic approach to alkene hydrogenation via stepwise outer-sphere hydrogen atom transfer (HAT) without M–C bond formation.^[6] HAT-based olefin hydrogenation (HAT-OH) can be coupled to radical isomerization, potentially offering new selectivities.^[5d,7,8] First-row transition metal hydride catalysts with medium to weak M–H bond strengths are typically employed.^[6b,9] A photoactive iridium hydride complex was recently used in photodriven HAT-OH after reductive excited state quenching.^[10] Furthermore, Chirik and co-workers reported a cobalt catalyst that switches from HAT-OH to an olefin insertion mechanism upon photolytic dissociation of a CO ligand.^[3k]

Shevick et al. recently discussed the scope of HAT-OH including some limitations based on the thermochemical framework.^[9] Typical low-spin hydride catalysts with strong field (SF) ligands exhibit M–H bond dissociation free energies (*BDFEs*) around 50–60 kcal·mol⁻¹, such as [CpCrH(CO)₃] (*BDFE*_{Cr–H} = 57 kcal·mol⁻¹ in MeCN).^[11] Therefore, the first HAT step to unactivated alkenes, like propylene, is thermodynamically quite unfavorable (*BDFE*_{C–H}(CH₃C[•]HCH₂-H) = 33 kcal·mol⁻¹; Figure 2, red), and overall hydrogenation is driven by the second HAT step.^[12,13,14] In consequence, HAT-OH of unactivated olefins, like propylene, with SF-ligand based catalysts is generally kinetically inaccessible at ambient conditions. Catalysts with weak M–H bonds (*BDFE*_{M–H} < 35 kcal·mol⁻¹) can be utilized instead,^[9] but require alternative reductants due to the high *BDFE* of H₂ (104 kcal·mol⁻¹ in toluene).^[6b,15]

A potential alternative approach could be provided by the use of dihydride catalysts, L_nMH₂, with distinctly lower M–H bond strength than the respective monohydride L_nMH (*BDFE*_{MH₂} < *BDFE*_{MH}). In that case, both HAT steps would be closer in reaction free energy (Figure 2, blue), rendering unactivated substrates more accessible while still being able to efficiently activate H₂, if the sum (*BDFE*_{MH₂} + *BDFE*_{MH}) is close to *BDFE*_{H₂}. However, as a possible pitfall such dihydride complexes would be thermodynamically unstable towards bimolecular H₂ evolution and formation of the catalytically inept monohydride, if *BDFE*_{MH₂} < 0.5 · *BDFE*_{H₂}.

To evaluate these considerations, a cobalt pincer platform like that reported by Choi and Lee (Scheme 1) provides an interesting starting point.^[16] The formation of a cobalt(II)

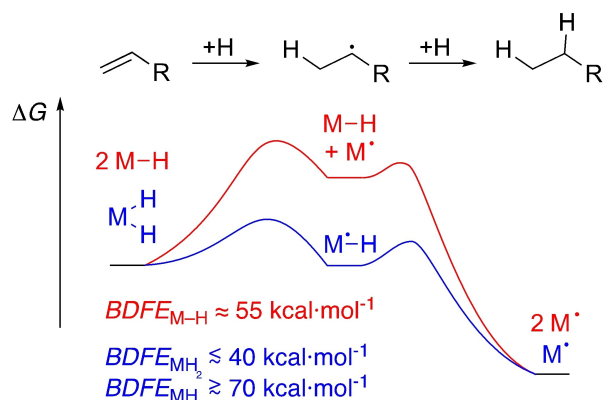
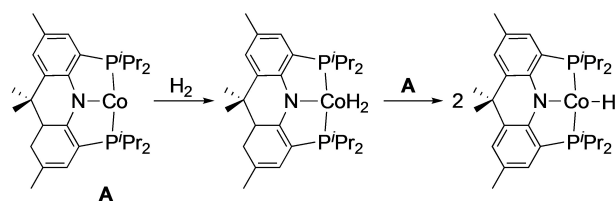


Figure 2. Thermochemical considerations for HAT-OH via mono- (red) and dihydride (blue) catalysts, respectively.



Scheme 1. Hydrogen activation by the cobalt pincer platform reported by Choi and Lee.^[16]

hydride complex from **A** was attributed to initial H₂ addition and subsequent comproportionation with parent **A**. This route suggests facile HAT reactivity of the H₂ adduct. Furthermore, the thermochemical boundary condition,

$$BDFE_{MH_2} < 0.5 \cdot BDFE_{H_2} < BDFE_{MH}$$

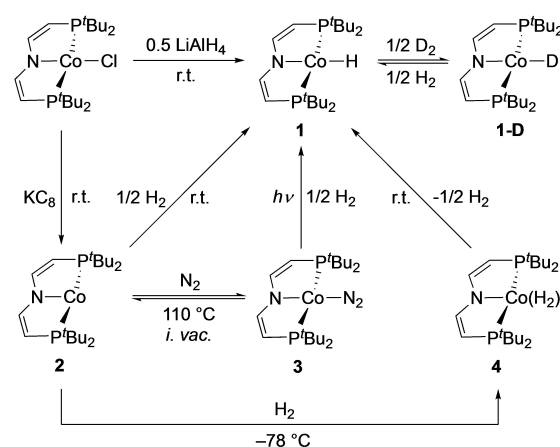
seems to be fulfilled. We here report a related cobalt(II) monohydride pincer complex, which is inactive for thermal olefin hydrogenation, but can be photolytically activated with visible light to catalyze photo-initiated HAT-OH of styrenes and also of unactivated, aliphatic alkenes.

Results and Discussion

Synthesis and characterization of [Co^{II}H(PNP)] (**1**); PNP = N(CHCHP^tBu₂)₂)

Starting from the previously reported chloride complex [CoCl(PNP)],^[17] the cobalt(II) hydride [CoH(PNP)] (**1**) can be prepared in over 70% isolated yield by salt metathesis with LiAlH₄ (Scheme 2). The analogous deuteride complex [CoD(PNP)] (**1-D**) was obtained with LiAlD₄ or, alternatively, by rapid H/D exchange of **1** under an atmosphere of D₂ in benzene (Scheme 2). The molecular structure of **1** in the crystal (Figure 3) resembles the metrical bonding parameters of the parent chloride complex.^[17] Slightly distorted square-planar coordination arises from the pincer bite angle (170.528(16)°). Compared with the chloride precursor (*d*_{Co–N} = 1.893(2) Å), the Co–N bond length of **1** (1.9369(12) Å) reflects the *trans*-influence of the hydride ligand, which could be located on the electron density map.

The Co–H stretching frequency of **1** ($\nu = 1756 \text{ cm}^{-1}$; $\Delta\nu_{H/D} = 487 \text{ cm}^{-1}$), ranges at the lower end when compared with other neutral cobalt(II) pincer hydride complexes (~1820–2030 cm⁻¹),^[31,18] reflecting a large *trans*-influence of the divinylamide ligand.^[19] The three paramagnetically shifted and broadened solution ¹H NMR signals of the pincer ligand support C_{2v}



Scheme 2. Synthesis of the cobalt complexes 1–4.

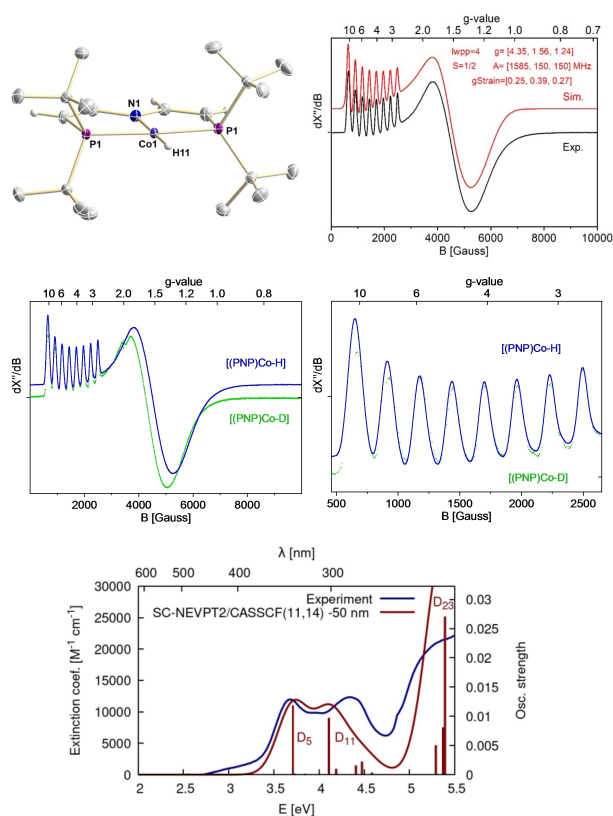


Figure 3. Top left: Molecular structure of **1** in the crystal from X-ray diffraction with the anisotropic displacement parameters drawn at the 50% probability level. ^tBu hydrogen atoms are omitted for clarity. Selected bond lengths (Å) and angles (°): Co1-H11 = 1.45(2); Co1-N1 = 1.9369(12); Co1-P1 = 2.2062(3); N1-Co1-H = 180.000(10); N1-Co1-P1 = 85.264(8); P1-Co1-P1 = 170.528(16). Top right: Experimental and simulated EPR spectra of **1** measured in toluene glass at 20 K (MW freq. = 9.6427, MW power = 0.6325 mW, Mod. amp. = 4 G). Middle: Overlays of the experimental EPR spectra of **1** and **1-D** (*g*-value scaled, normalized). Bottom: Comparison of the experimental electronic absorption spectrum of **1** in THF (blue, -95 °C) with the computed one (red, SC-NEVPT2/CASSCF(11,14)/def-TZVP) for the PMe₂ truncated model, shifted by -50 nm.

symmetry on the NMR timescale. A ¹H NMR signal for the hydride ligand was not found.

The room temperature solution magnetic moment in C₆D₆ ($\mu_{\text{eff}} = 1.97 \pm 0.27 \mu_{\text{B}}$) and the temperature dependent susceptibility measurements of a powdered sample (see Supporting Information) are both in agreement with an electronic low-spin configuration (*S* = 1/2) with a sizable orbital momentum (*g*_{iso} = 2.84 for powdered sample). This is further supported by X-band EPR spectroscopy in toluene at 20 K (Figure 3), which could be satisfactorily fitted with a rhombic, highly anisotropic *g*-tensor (*g* = 4.35, 1.56, 1.24; $\langle g \rangle = 2.76$) and large ⁵⁹Co hyperfine interaction (HFI) for the low-field component (*A*₁ = 1585 MHz). The EPR data support metal-centered radical character and resemble the related cobalt(II) PNP pincer hydride complex [CoH{NC₅H₃(CHP^tBu₂)(CH₂P^tBu₂)}] reported by Chirik and co-workers.^[18a] Large ⁵⁹Co HFI and *g*-anisotropy are generally found for square-planar, low-spin cobalt(II) due to pronounced mixing of the ground state with low-lying excited states mediated by spin-orbit coupling.^[18a,20,21] Multiconfigurational SC-NEVPT2/

CASSCF(11,14) computations of a PMe₂-truncated model of complex **1** indicated that the ground state is dominated by the (3d_{xy})²(3d_{yz})²(3d_{z²})¹(3d_{xz})² doublet configuration (88%), where the 3d_{x²-y²} orbital contributes to form the Co–H σ and σ* orbitals with an atomic contribution of ca. 60% in both molecular orbitals. Calculations with this PMe₂-truncated model already reproduce the large *g*-anisotropy (*g* = 4.80, 1.50, 1.25) satisfactorily.

The UV/vis spectrum of **1** recorded in THF at -95 °C (Figure 3) exhibits intense bands at 285 nm ($\epsilon = 1.2 \cdot 10^4 \text{ M}^{-1} \cdot \text{cm}^{-1}$) and 337 nm ($\epsilon = 1.2 \cdot 10^4 \text{ M}^{-1} \cdot \text{cm}^{-1}$). These absorptions are qualitatively reproduced by the SC-NEVPT2/CASSCF(11,14) computations that included the low-lying 4p_z orbital in the active space. Accordingly, we assign the bright state at 337 nm to the D₅ doublet state (Figure 3 and Table S3), mainly composed of the (3d_{xy})²(3d_{yz})²(3d_{z²})¹(3d_{xz})¹(4p_z)¹ configuration (62%) with the (dipole allowed) excitation to the 4p_z orbital, another (12%) configuration with an excitation to the 4p_z orbital and a smaller contribution (8%) of an excitation to the Co–H σ* antibonding orbital with (3d_{xy})²(3d_{yz})²(3d_{z²})²(3d_{xz})⁰(σ*)¹ configuration. The bright state at 294 nm is also a mixture of doublet configurations: 36% and 32% of configurations involving 3d → 4p_z excitations and 11% of a 3d → σ* configuration (see Table S3). In all of them, the 3d_{x²-y²}

orbital participates in the Co–H σ orbital and remains doubly occupied. Besides these strong absorptions, a broad band at 522 nm with low intensity ($\epsilon = 124 \text{ M}^{-1} \cdot \text{cm}^{-1}$) was found in the UV-vis spectrum in benzene (Figure S2). The SC-NEVPT2 computations predict a quartet state (Q₃ in Table S3) in this region, which is expected to borrow intensity via spin-orbit coupling.

Interestingly, the ¹H NMR spectrum of the deuteride isotopologue **1-D** exhibit a noticeable isotopic shift of up to 1 ppm for one set of methyne protons in the pincer backbone. Pronounced NMR isotope effects on remote nuclei, sometimes called paramagnetic isotope effect on chemical shift (PIECS),^[22f] were previously reported for several paramagnetic molecules,^[22] including some multinuclear, hydride bridged complexes.^[22f-i] In that case, PIECS was attributed to the slightly shorter M–D bond lengths, resulting in increased exchange coupling of the open-shell metal ions. However, in the current, mononuclear case, the isotope effect of the hyperfine shift must be associated with a perturbation of the ligand field upon Co–H/D exchange. In fact, EPR characterization of **1-D** (Figure 3) supports a ligand field effect as origin of PIECS, as expressed by the slightly smaller *g*-anisotropy (*g* = 4.29, 1.62, 1.29) and ⁵⁹Co HFI in the low-field component (*A*₁ = 1570 MHz). The non-equal PIECS contributions for the two pincer backbone ¹H NMR signals suggest a contribution from dipolar coupling, which is in agreement with the large anisotropy of the *g*-tensor.^[23] We tentatively associate the isotope effect with the distinct multi-reference character of the ground state, as a shorter Co–D bond is expected to perturb contributions from configurations with the filled d_{x²-y²} orbital.

Synthesis and characterization of [Co(L)(PNP)] (L = none (2), N₂ (3), H₂ (4))

Reaction of the chloride precursor with LiHBEt₃ as hydride source, primarily leads to reduction, as reported by Chirik and co-workers for related Co pincer complexes.^[24] However, the cobalt(I) compounds [Co(L)(PNP)] (L = none (2), N₂ (3)) are more conveniently prepared by reduction with K_{C₈} under Ar or N₂, respectively (Scheme 2). The [Co(PNP)] platform exhibits extremely high nitrogen affinity and 3 is obtained in the presence of only traces of dinitrogen. N₂-binding is reversible and 2 can be obtained from 3 by sublimation at 110 °C (10⁻³ mbar).

The molecular structure of the square-planar dinitrogen complex 3 was confirmed by X-ray diffraction (Figure S49). The closed-shell complex exhibits the typical NMR signature ($\delta_p = 81.6$ ppm) of diamagnetic, C_{2v} symmetric complexes with this divinylamido PNP pincer ligand. The N₂ stretching vibration ($\nu_{N=N} = 2012$ cm⁻¹) indicates weak activation. In contrast to complex 3, strongly paramagnetically shifted and broadened ¹H NMR signals support an electronic triplet ground state for 2, as was previously reported for other T-shaped three-coordinate cobalt (I) complexes.^[3h,25] DFT computations confirm this notion, predicting that the triplet (*S* = 1) ground state of [Co(PNP)] is 20 kcal·mol⁻¹ below the singlet (*S* = 0, see Supporting Information, Section 8.1). Notably, Lee's 3-coordinate cobalt(I) PNP pincer complex (Scheme 1, A) was reported to exhibit a low-spin ground state.^[16] Unfortunately, the extremely high N₂ affinity of 2 so far prevented reliable combustion analysis and thus magnetic characterization.

While the dinitrogen complex 3 is thermally stable under H₂ (1 atm in C₆D₆), the monohydride 1 is selectively formed upon photolyzing ($\lambda_{exc} = 390$ nm) this mixture (Scheme 2). In contrast, complex 2 directly gives 1 (and minor amounts of 3 from residual N₂) with H₂ (1 atm) over the course of several hours at r.t., reflecting the work from Choi and Lee (Scheme 1).^[16] Notably, at -70 °C in d₈-toluene, a diamagnetic product ($\delta_p = 96.3$ ppm) was selectively obtained. A ¹H NMR signal at -28.5 ppm (²J_{HP} = 74.2 Hz), which integrates over two protons, supports the initial formation of [CoH₂(PNP)] (4) as a cobalt(III) dihydride or cobalt(I) dihydrogen complex.^[3i,16,26,27] Under HD (0.7 atm) at -100 °C (Figure S17), the linewidth of the hydride NMR signal (39 Hz) did not allow for unequivocal differentiation. Furthermore, a statistical mixture of H₂/HD was observed, indicating rapid H/D scrambling already at very low temperatures. Warming to room temperature resulted in selective conversion of 4 to paramagnetic 1 (Scheme 2), which confirmed that 4 is an intermediate but also impeded structural assignment based on the T₁ criterion.^[3j] Computational examination of 4 by DFT supports the dihydrogen isomer with a computed H...H distance of 0.94 Å (Figure S45). The computations also revealed a Co–H bond strength (*BDFE*_{CoH₂} = 37 kcal·mol⁻¹; Figure 4 Top)^[28] that is distinctly lower than that of the monohydride HAT product 1 (*BDFE*_{CoH} = 62 kcal·mol⁻¹), which is in line with the decay of 4 to 1 and 0.5 equiv. H₂ (0.5·*BDFE*_{HH} = 52 kcal·mol⁻¹).

The mechanism of the formation of 1 was examined by monitoring the H₂ pressure dependence (2–4 bar) of the decay

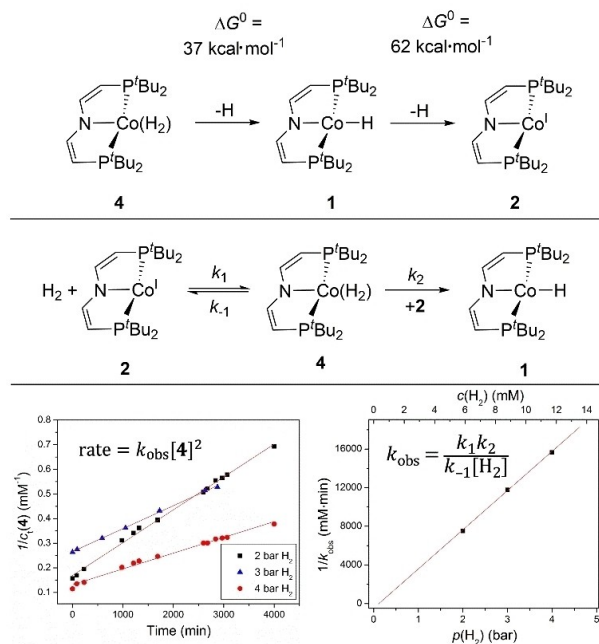


Figure 4. Top: Computed *BDFE*_{CoH₂} of 4 and *BDFE*_{CoH} of 1. Middle: Mechanistic model for the conversion of 2 to 1 with H₂. Bottom: H₂-pressure dependent kinetic data for the decay of 4.

of 4 with ¹H NMR spectroscopy (Figure 4, Bottom). The reaction rate follows second order dependence in [4] and inverse dependence of *k*_{obs} on H₂ pressure with a zero-intercept of the *k*_{obs}⁻¹ vs. *p*(H₂) plot. These findings are in agreement with a rapid pre-equilibrium of 2 and H₂ with 4 that is followed by comproportionation via formal HAT (Figure 4, Middle and Supporting Information, Section 3.8). Third-order rate laws (*r* = *k*·[M]²·[H₂]) were previously reported for the addition of H₂ across two metal atoms (2 M + H₂ → 2 MH).^[29] Notably, Wayland and Sherry associated a small kinetic isotope effect with a termolecular reaction via a linear {M...H...H...M} transition state.^[29b] However, Hoff attributed small enthalpies of activation observed for several compounds to a stepwise reaction with initial, enthalpically driven H₂ binding to one metal ion,^[30] as represented by the mechanism of Choi and Lee (Scheme 1).^[16] Our spectroscopic and kinetic results fully support such a stepwise pathway via an H₂ binding preequilibrium.

Photochemical activation of [CoH(PNP)] (1)

The strong Co–H bond of monohydride 1 obviously demands additional activation to initiate efficient HAT-based catalysis. Photolytic M–H homolysis has been reported for several transition metal hydrides,^[31] motivating the examination of the photochemistry of 1. In the dark, hydride 1 exhibits high chemical stability. No reaction was observed over the course of several days at 60 °C in C₆D₆. In contrast, photolysis in C₆D₆ at r.t. near the low energy edge of the strong absorption bands (LED, $\lambda_{exc} = 390 \pm 20$ nm) under a static vacuum^[32] resulted in

slow ($k_{\text{obs}} \approx 1.1 \cdot 10^{-3} \text{ h}^{-1}$) conversion to 1-D, as confirmed by the PIECS-induced ^1H NMR shift, mass spectrometry and IR spectroscopy (Figure 5). Approximately equimolar generation of $\text{C}_6\text{D}_5\text{H}$ confirmed H/D exchange with the solvent (Figure S19). In addition, trace quantities of complex 2 ($\sim 5\%$) were rapidly formed but did not further accumulate during photolysis. A low quantum yield of $\Phi_{390} = 0.097\%$ was derived for the photolytic H/D exchange reaction with d_6 -benzene.

The steady state H/D exchange experiment suggests initial photolytic Co–H bond cleavage. M–H photofragmentation was first examined within closed-shell hydride carbonyl complexes by matrix isolation techniques.^[33] Multiconfigurational computations of these systems have attributed HAT with excited state crossings that lead to a dissociative triplet surface.^[34] However, besides M–H homolysis, the photolysis of hydride complexes can also lead to net proton or hydride transfer, respectively,^[31] sometimes even for the same compound. For example, Fukuzumi and Guldi showed that the $^3\text{MLCT}$ excited state of Ziesse's photocatalyst $[\text{Cp}^*\text{IrH}(\text{bipy})]$ ^[35] undergoes facile proton transfer to MeOH,^[36] while Miller and co-workers reported photochemical H_2 evolution in MeCN via a photo-driven disproportionation mechanism.^[37] In view of the rich photochemistry of hydride complexes, the scarcity of transient absorption studies is quite surprising.^[3k,10,36,38,39]

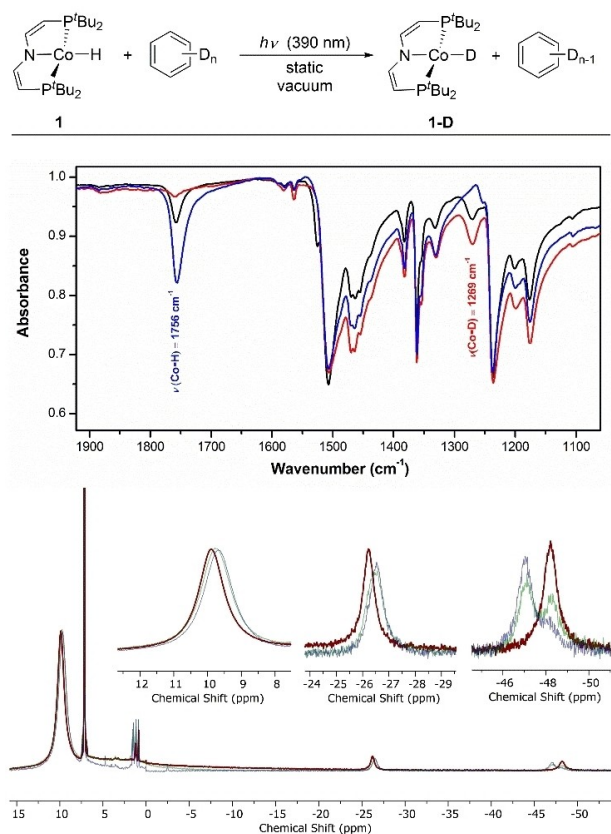


Figure 5. Top: Reaction conditions for photo-induced H/D exchange of 1 and C_6D_6 . Middle: ATR-IR spectra of solid 1 (red), 1-D (blue) and 1 after photolysis in C_6D_6 for 36 h (black). Bottom: ^1H NMR spectra of 1 in C_6D_6 before (red) and after photolysis for 20 h (green, 53% yield) and 36 h (blue, 81% yield).

Both the cobalt(II) hydride (1) and deuteride complexes (1-D) were therefore examined by UV/mIR spectroscopy in liquid *n*-hexane solutions. A selection of experimental pump-probe spectra of 1-D recorded at various representative time delays is depicted in Figure 6. Two relatively strong negative bands are observed at 1235 cm^{-1} and 1511 cm^{-1} , i.e. exactly at the spectral positions of the C–H in-plane bending and the C=C stretching modes of the PNP pincer ligand. These signals indicate an increase of the sample's transmission and arise from the electronic excitation of 1-D and the concomitant depletion of population in its electronic ground state. Each of these two ground state bleaches (GSBs) is accompanied by a slightly downshifted transient absorption (TA). Immediately after absorption of the pump photon, i.e. at a time delay of zero, the optically prepared excited electronic state is the most obvious species, which can be held accountable for the induced absorptions. Finally, a third but much weaker GSB band is observed that is maximal at 1285 cm^{-1} , and hence, is due to the Co–D stretching vibration. Notice that there is again an accompanying TA-band peaking at 1246 cm^{-1} whose low-

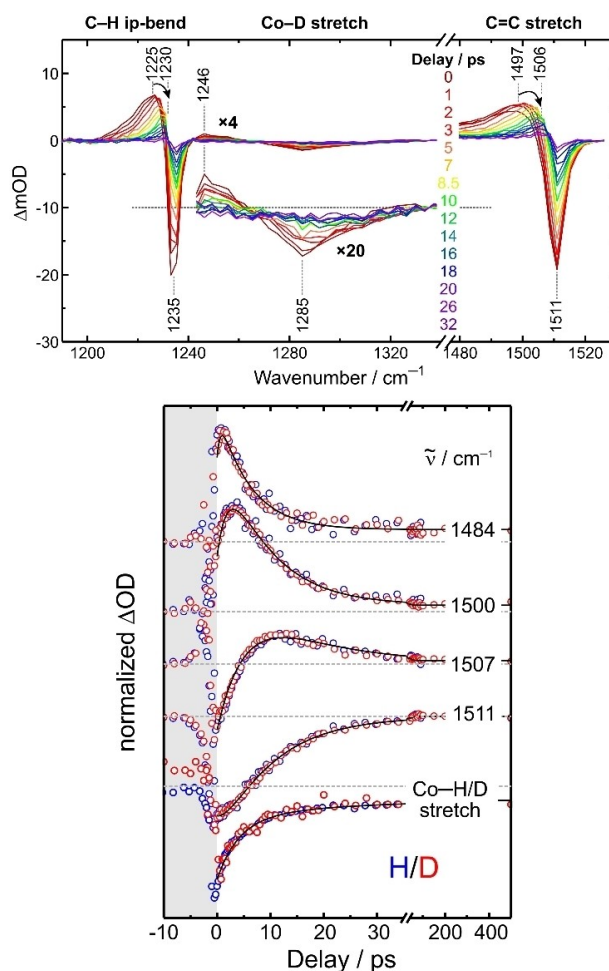


Figure 6. Top: Time resolved UV-pump mid-IR-probe spectra of 1-D in *n*-hexane following 400 nm-excitation and probing the spectral regions of C–H in-plane bending (left), the Co–D stretching (middle), and C=C stretching (right) modes. Bottom: Comparison of kinetic traces of 1 and 1-D.

frequency edge is likely obscured by the nearby, much stronger GSB of the C–H in-plane bend. Importantly, the existence of an induced absorption in the Co–D stretching region is sufficient evidence that the species responsible for the TA-bands in Figure 6 has an intact Co–D bond. At a time delay of zero, this finding supports the notion of an optically prepared excited state of **1** that is bound with respect to the Co–D stretching coordinate. Note also that except for the isotope shift of the deuteride stretching bands, qualitatively very similar results were obtained for **1** (Figure S44).

The TA-bands associated with the pincer modes are significantly broader than their corresponding GSB-bands. In addition, they progressively shift to higher wavenumbers and spectrally narrow as the time delay is increased. These observations suggest that a significant fraction of the pump photon energy is effectively converted into excess kinetic energy residing in the system's vibrational modes and that the complex vibrationally relaxes on a time scale of a few picoseconds.^[40] Finally, the band integrals of the three induced absorptions decay with increasing delay while simultaneously the bleaching bands fade away. As the system vibrationally cools, the population of the electronic ground state gradually recovers within a few tens of picoseconds. Kinetic traces for selected probe wavenumbers (Figure 6) of both, **1** (blue) and **1-D** (red) reveal a complicated temporal evolution due to the superposition of vibrational cooling and ground state recovery. Therefore, the traces can only be fitted in a purely phenomenological fashion using multi-exponential kinetics (solid curves in Figure 7). Clearly, both isotopologues feature identical traces at corresponding probe wavenumbers, which rules out any significant kinetic isotope effect. All traces practically decay to zero at infinite delays indicating (near) quantitative recovery of the ground-state population without significant photochemical conversion. The absence of a residual GSB corroborates the results from H/D scrambling with C₆D₆ under static photolysis, which proceeds with low quantum yields.

To rationalize the photochemistry, the solvent was changed to liquid benzene-*h*₆, now employing broadband white-light probing of electronic transitions after the optical excitation at 400 nm. Figure 7a displays such UV/nUV-vis spectra of **1-D** for time delays that are complementary to those from Figure 6. Following the absorption of the pump pulse, two distinct induced transient absorption bands peaking near 540 nm and 460 nm are observed and maybe a third, slightly weaker band around 650 nm. The ensuing spectro-temporal dynamics of the two major bands appear to be markedly different as evidenced by a reversal of their relative amplitudes. Whereas the 540 nm-band is the dominant component at early delays, only the band at shorter wavelength prevails for delays in excess of 10 ps. In addition, both bands experience a subtle dynamic blue-shift with increasing delay (cf. gray arrows in Figure 7a), which may be linked to the same dynamics of vibrational relaxation already seen in the femtosecond mIR-spectra.

In contrast to the mIR-data, however, the UV/nUV-vis spectra reveal a very faint residual transient absorption that appears to be stationary from ~70 ps onwards and may therefore be attributed to a primary photochemical product. To

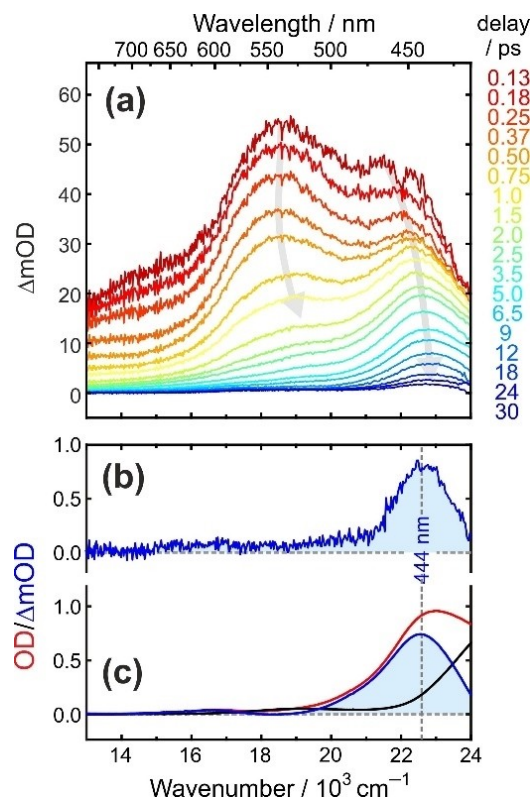


Figure 7. a) Femtosecond vis-to-near-UV transient spectra of **1-D** in liquid benzene-*h*₆ solution at room temperature. b) Experimental photoproduct spectrum. c) Stationary UV/vis-spectrum of **1** (black curve) and **2** (red curve). The blue spectrum is the difference spectrum, **2**–**1**.

characterize this asymptotic absorption with a satisfactory signal-to-noise ratio all transient spectra recorded between 70 and 150 ps were averaged into a “final” photoproduct spectrum, the result of which is displayed in Figure 7b (blue curve). This spectrum contains only a single band that is centered at 444 nm. Its amplitude is a factor of 10² smaller than that of the UV/nUV-vis-spectrum recorded at zero time delay, which is again suggestive of a very small quantum yield of the order of ≤1%. Most importantly, the experimental spectrum is reminiscent of the stationary electronic absorption spectrum of **2**, which exhibits a characteristic absorption band centered at 435 nm (Figure 7c). The shift of the pump-probe spectrum by 9 nm as well as the absorption depletion on the high-frequency edge at 420 nm relative to the stationary spectrum can be attributed to the onset of the GSB of **1**. The latter, in turn, is given by the inverted stationary absorption spectrum of **1**. If the only photochemical pathway is the formation of **2**, the “final” photo-product spectrum is simply given by the difference between the red and the black spectra shown in Figure 7c. In fact, the resultant difference spectrum (blue curve) agrees remarkably well with the experimental spectrum of **2**. Due to the low quantum yield of **2**, no unambiguous conclusions can be drawn regarding the dynamics of its formation.

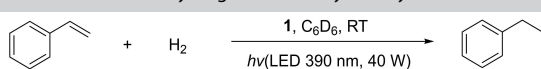
Photo-initiated olefin hydrogenation

The photoactivation of monohydride complex **1** can be coupled to H₂ activation. For example, photolysis of **1** (10.6 mM, 390 nm LED) in benzene or toluene under a D₂ atmosphere (1 bar) gives around 3 turnovers for aromatic C–H deuteration over the course of 40 h. Motivated by these results, olefin hydrogenation was examined next, using styrene as a benchmark substrate. With 10 mol% loading of **1** (Table 1, entry 1), quantitative hydrogenation of styrene to ethylbenzene was observed upon photolysis (LED, 390 nm) over 15 h at r.t. under 1 bar H₂. Notably, with 5 mol% **1** a quantum yield of $\Phi_{390} = 2.29\%$ was obtained, which is more than an order of magnitude higher than the H/D isotopic exchange reaction with benzene. Addition of Hg (Table 1, entry 2) does not affect the reactivity, supporting homogeneous catalysis. No conversion is obtained in the absence of light (Table 1, entry 3). Lower catalyst loadings (entry 4) led to reduced yields. In turn, increased H₂ pressures afforded higher catalytic rates, enabling quantitative hydrogenation with 1 mol% catalyst loading (Table 1, entries 5–8).

Photo-HAT-OH catalyzed by [Cp*IrH(phen)] (5 mol%, 44 h, 50 °C, 470 nm; reductant: NEt₃) exhibits a preference for 1,1-disubstituted arylalkenes.^[10] Aliphatic substrates generally gave low yields and considerable amounts of 1,2-isomerization to internal alkenes. This selectivity parallels HAT rates of [CpCrH(CO)₃], which follow the thermochemical stability of the formed alkyl radical with rate retardation for sterically encumbered olefins.^[7] For comparison, the reaction scope with catalyst **1** was examined (Table 2). Using a standard protocol (10 mol% **1**, 390 nm LED, 15 h, r.t. 1 bar H₂), styrenes with both electron withdrawing and donating *para*-substituents (Table 2, entries 1–4) were quantitatively hydrogenated. 1,1-Disubstituted olefins (Table 2, entries 5 and 6) exhibited incomplete conversion even at increased reaction times.

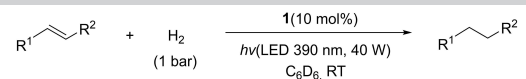
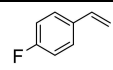
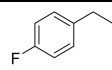
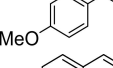
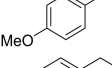
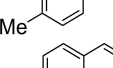
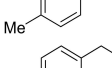
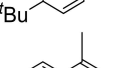
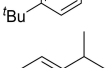
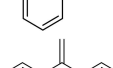
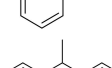
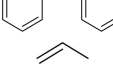
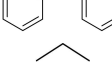
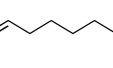
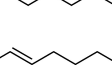
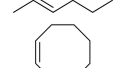
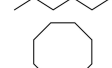

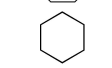
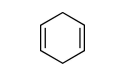
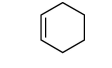

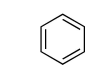
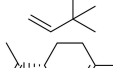
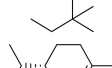
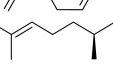
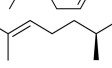
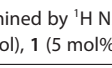
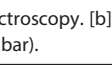
Notably, aliphatic α -olefins are rapidly consumed, contrasting with the trends found for [Cp*IrH(phen)]. In fact, propene was almost quantitatively hydrogenated, at 5 mol% catalyst loading and 2 bar H₂ (entry 7). For the longer chain α -olefins, like 1-octene (Table 2, entry 8), significant isomerization to 2-octene (25%) was observed. This is in line with the low hydrogenation rates found for internal olefins, such as 2-hexene, cyclooctene, or cyclohexadiene (Table 2, entries 9–11).

Table 1. Photo-induced hydrogenation of styrene by **1**.

				
Entry	Cat [mol%]	H ₂ Pressure [bar]	t [h]	Yield (conversion) [%] ^[a]
1	10	1	15	100
2 ^[b]	10	1	15	100
3 ^[c]	10	1	15	0
4	5	1	15	68 (68)
5	5	4	15	100
6	5	8	15	100
7	1	4	15	62 (63)
8	1	8	15	100

[a] Determined by ¹H NMR spectroscopy. [b] In the presence of Hg. [c] Without irradiation.

Table 2. Photo-induced hydrogenation of styrenes and aliphatic olefins by **1**.

				
Entry	Substrate	Product	t [h]	Yield (conversion) [%] ^[a]
1			15	100
2			15	100
3			15	100
4			15	100
5			15	39 (41)
6			40	51 (53)
7 ^[b]			15	92 (93)
8			15	75 (octane) 25 (2-octene)
9			40	32 (33)
10			15	37 (37)
11			40	62 (C ₆ H ₁₀) 15 (C ₆ H ₁₂) 12 (C ₆ H ₆) (90)
12			15	66 (67)
13			15	20 (22)
14			26	100

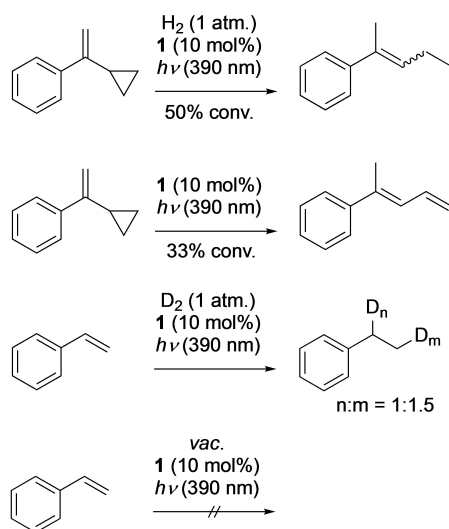
[a] Determined by ¹H NMR spectroscopy. [b] Conditions: substrate (1.5 bar, 0.042 mmol), **1** (5 mol%), H₂ (2 bar).

As for the aromatic substrates, we attribute this selectivity to steric reasons, exemplified by bulky (Table 2, entry 12) and branched (Table 2, entry 13) α -olefins, or completely inert 1,1,2-trisubstituted substrates (Table 2, entry 13). Apparently, the same steric considerations apply to 1,2-isomerization: The terminal double bond of 3,7-dimethyl-1,6-octadiene to 2,6-dimethyl-2-octene (entry 14) was quantitatively and selectively hydrogenated under these conditions within 26 h. Importantly, except for isomerization, selectivities were quantitative within error in all cases.

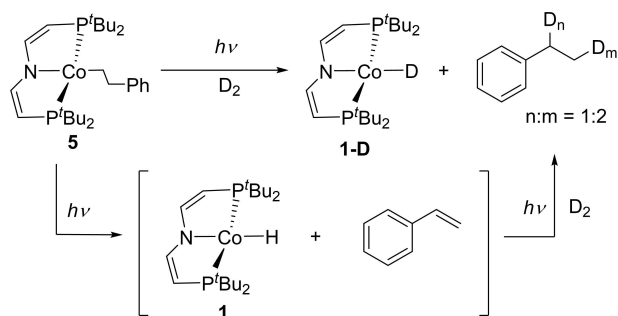
Mechanistic examinations

The nature of the hydrogenation reaction was examined with the radical-clock substrate α -cyclopropylstyrene under standard conditions (10 mol% **1**, 390 nm LED, 1 bar H_2). Selective hydrogenation to the ring-opened product 2-phenyl-2-pentene is observed (Scheme 3). This finding supports a radical mechanism via initial HAT and subsequent ring opening of the resulting tertiary alkyl radical, which proceeds with a unimolecular rate constant of $k = 3.6 \cdot 10^5 \text{ s}^{-1}$ at 22 °C.^[41] In the absence of H_2 , this substrate is isomerized to 4-phenyl-1,3-pentadiene, yet with slightly lower rates. Catalytic styrene reduction with D_2 results in higher deuterium incorporation at the primary site of the product ($D_\alpha:D_\beta = 1:1.5$), suggesting reversibility of the first HAT step, as was observed for carbonyl hydride complexes, which undergo HAT mediated, thermal H/D exchange with olefins.^[6a,7]

The nature of the active catalyst species was examined by stoichiometric and catalytic control experiments. Hydride **1** and styrene do not react in the absence of light. The short excited-state lifetime precludes direct bimolecular excited-state reactivity. Furthermore, photolysis of **1** and styrene under vacuum (Scheme 3) confirms that hydrogenation requires the presence of H_2 . An olefin insertion mechanism was probed by examina-



Scheme 3. Mechanistic control experiments.



Scheme 4. Styrene deuteration with complex **5**.

tion of $[Co(CH_2CH_2Ph)(PNP)]$ (**5**; Scheme 4), which was prepared by salt metathesis from the chlorido complex. **5** does not react with H_2 under thermal conditions. However, photolysis (390 nm LED) under Ar converts **5** to **1** and styrene, while **1** and $Ph(CH_2, \dots, nD_n)(CH_3, \dots, mD_m)$ are obtained under D_2 , respectively. Importantly, the isotopic distribution in the deuteration product ($n:m \approx 1:2$) resembles that of catalytic styrene deuteration with **1**. These observations are in line with initial photochemical styrene extrusion from **5** (Scheme 4), disfavoring the hydrogenolysis of the cobalt(II) hydrocarbyl intermediate as a relevant step for catalysis.

These control experiments indicate that HAT-OH is initiated by the formation of a photoproduct that activates H_2 as first step in catalysis. Along these lines, the considerably higher quantum yield for styrene hydrogenation than for H/D scrambling with the solvent is suggestive of thermal HAT-OH, which is catalyzed by an *in situ* formed photoproduct. In fact, initial photochemical styrene hydrogenation with **1** for 1 h and subsequent monitoring without irradiation (Figure 8) revealed catalytic ethylbenzene formation in the dark, yet with lower reaction rates. We therefore turned to the examination of **2**, which is the product of both steady state and time resolved photolysis of **1** (see above). Unlike H_2 , styrene does not bind to **2**, presumably for steric reasons. Styrene hydrogenation (2 mol% **2**, 1 bar H_2 , r.t.) without simultaneous photolysis confirmed that complex **2** is, in fact, a thermal catalyst (Figure 8). Catalytic rates gradually slow down on a timescale that is consistent with the decay of **4** to **1**, which is inactive as a thermal catalyst. As shown by the kinetic examinations (Figure 4), the deactivation rate is second order in **4**. We therefore examined initial turn-over frequencies at different catalyst loadings (1 bar H_2 , 390 nm, r.t.). With 5 mol% **1**, turn-over after 3 h ($TOF_3h = 0.7 \text{ h}^{-1}$) was considerably lower than with 1 mol% (3.4 h^{-1}), supporting that catalyst deactivation has a higher reaction order in cobalt than competing hydrogenation.

Our results support the proposed mechanism shown in Scheme 5. Photolysis of **1** results in Co-H homolysis as the activating step. After H_2 addition, the dihydrogen complex **4** is

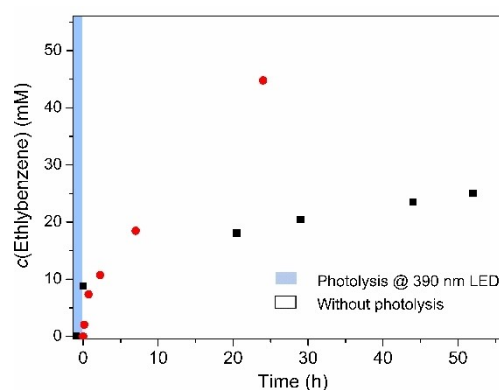
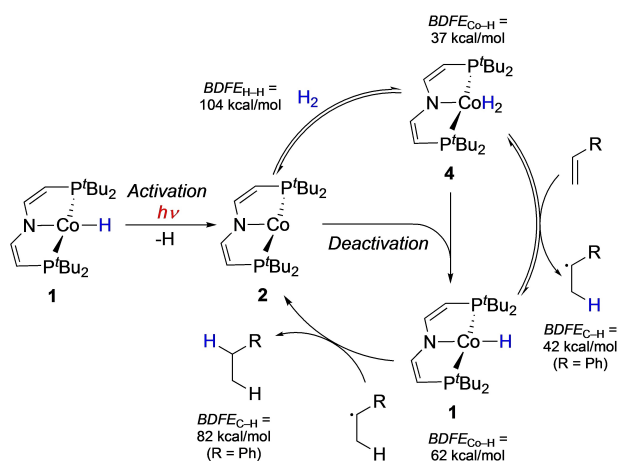


Figure 8. Time dependent ethylbenzene formation by catalytic hydrogenation of styrene (0.048 mmol, 1 bar H_2) using either **1** (black squares) with 1 h photolysis (blue shaded area) and subsequent reaction without irradiation, or isolated **2** (3.8 mol%, red circles) as catalysts.



Scheme 5. Proposed mechanism for photo-initiated HAT-OH with 1.

a thermal HAT-OH catalyst. The computational evaluation confirmed distinctly different $BDFEs$ for the two hydrogen atoms bound to the metal. The low Co–H bond strength of 4 ($BDFE_{\text{CoH}_2} = 37 \text{ kcal}\cdot\text{mol}^{-1}$) is close to the C–H bond strength of the α -methylbenzyl radical ($BDFE_{\text{CH}} \approx 42 \text{ kcal}\cdot\text{mol}^{-1}$ in toluene),^[13,42] as a basis for facile and reversible initial HAT of 4 to styrene, but also to aliphatic, unactivated olefins. HAT from 4 to the olefin gives parent 1 ($BDFE_{\text{CoH}} = 62 \text{ kcal}\cdot\text{mol}^{-1}$), which is insufficient to undergo direct HAT to styrene, but to the alkyl radical producing a strong C–H bond (ethylbenzene: $BDFE_{\text{CH}} \approx 82 \text{ kcal}\cdot\text{mol}^{-1}$ in toluene).^[13,43] Concomitant regeneration of 2 closes the proposed catalytic cycle.

Deactivation of the catalytic cycle could result from different processes. The low $BDFE_{\text{CoH}_2}$ of 4 renders comproportionation with 2 to inactive 1 thermochemically feasible and was shown as stoichiometric, pressure dependent decay path (Figure 4). Continuous photolysis maintains a steady state concentration of 4 that enables thermal catalysis. We attribute the higher catalytic rates at increased H_2 pressures to higher steady state concentrations of active catalyst 4. Deactivation could also arise by HAT from 4 to the α -methylbenzyl radical that escaped from the solvent cage after the first HAT. However, the low primary quantum yields for the photoactivation of 1 suggest low steady state concentrations of 2 and 4.

Conclusions

In this proof-of-principle study, a complementary approach to HAT-OH was evaluated. Based on thermochemical arguments, Holland, Shenvi and co-workers distinguished between two types of catalysts that define the scope and chemoselectivity: (a) Hydride complexes with strong field (SF) ligands and low-spin configuration ($BDFE_{\text{MH}} = 50\text{--}60 \text{ kcal}\cdot\text{mol}^{-1}$) enable the reduction of activated substrates with H_2 , vs. (b) hydrides with weak ligand fields (WF) in higher spin states ($BDFE_{\text{MH}} < 35 \text{ kcal}\cdot\text{mol}^{-1}$), which allow for the hydrogenation of unactivated alkenes with alternative reductants. We would like to

amend this scheme by SF dihydride (or dihydrogen) complexes with distinctly lower $BDFE_{\text{MH}_2}$ than the $BDFE_{\text{MH}}$ of their respective monohydride HAT product. This thermochemical framework enables, besides facile radical hydrogenation of styrenes, the hydrogenation of unactivated, aliphatic olefins, which is attributed to the increased driving force for the first HAT step giving the thermochemically unfavourable alkyl radical.

A challenge that has to be overcome arises from the relative bond strengths $BDFE_{\text{MH}_2} < 0.5 \cdot BDFE_{\text{H}_2} < BDFE_{\text{MH}}$, which favours the formation of the catalytically inactive monohydride. We demonstrated that photochemical M–H homolysis is a possible strategy for catalyst (re-)activation. The stationary photolysis and transient absorption data show that excitation of 1 with blue light ($\lambda = 400 \text{ nm}$) gives the cobalt(I) complex 2 as the direct photoproduct. The observation of a Co–H/D stretching absorption in the IR pump-probe spectrum at a time delay around $t = 0$ suggests that the electronic excitation does not directly populate a dissociative state. Unfortunately, more detailed analysis of the excited state dynamics was hampered by the low quantum yields ($\Phi_{400} < 1 \%$), which in turn may reflect that the photon energy ($71 \text{ kcal}\cdot\text{mol}^{-1}$) is close to the energy required for Co–H homolysis ($BDFE_{\text{CoH}} = 62 \text{ kcal}\cdot\text{mol}^{-1}$).

The spectroscopic and computational data support the formation of the low-spin cobalt(I) dihydrogen complex 4 with low $BDFE_{\text{CoH}_2}$ ($37 \text{ kcal}\cdot\text{mol}^{-1}$) after addition of H_2 to the three-coordinate photoproduct 2. The decay of 4 proceeds by comproportionation with parent 2 via formal HAT as supported by the distinct pressure dependence. Peters and co-workers recently associated the dihydrogen character of a trisphosphinoborane $\{\text{Co}^0\text{H}_2\}$ complex with outer-sphere HAT reactivity to a hydrogen atom acceptor.^[27g] In turn, Fout and co-workers showed for a cobalt pincer hydrogenation catalyst that the cobalt(I) dihydrogen resting state isomerizes to a cobalt(III) dihydride upon olefin coordination.^[3g] At the current point, our level of mechanistic understanding does not provide comprehensive structure/reactivity relationships for the formal HAT reactivity of 4 and 1. However, it is likely that the bulky pincer ligand supports outer-sphere HAT catalysis by preventing olefin binding that leads to full H_2 oxidative addition as an entry to an insertion-based pathway. Notably, Hanson's catalyst that carries a PCy_2 substituted, saturated analogue of our pincer ligand was proposed to operate via an inner-sphere mechanism.⁴ Steric shielding might also be instrumental to prevent the formation of multinuclear PNP-bridged hydrides, as observed by Arnold's and Mindiola's groups.^[44] Besides mechanistic predictors, the scope and activity of such photo-assisted HAT-OH dihydride catalysts need to be advanced in future work.

Experimental Section

Materials and methods: All experiments were performed under inert conditions using standard Schlenk and glove-box techniques under argon atmosphere. Photolysis experiments were carried out using a Kessil PR160-390 LED (390 nm, 40 W) while keeping the sample at room temperature by a water bath. Solvents were purchased in HPLC quality (Sigma Aldrich) and dried using an MBraun Solvent Purification System. THF was additionally dried

over Na/K. Deuterated solvents were obtained from Deutero GmbH and dried over Na/K (benzene- d_6 , THF- d_8 , Tol- d_8). 1-Cyclopropylvinylbenzene was synthesized according to a reported procedure.^[45] All other chemicals were used as received: Styrene (TCI), 4-fluorostyrene (TCI), 4-methylstyrene (Sigma Aldrich), 4-methoxystyrene (Sigma Aldrich), 4-tert-butylstyrene (TCI), propene (Sigma Aldrich), 1,4-cyclohexadiene (Sigma Aldrich), cyclooctene (Sigma Aldrich), trans-2-hexene (Thermo Fischer), 1-octene (Sigma Aldrich), (*R*)-(+)-limonene (Sigma Aldrich), (+)- β -citronellene (Sigma Aldrich), 1,1-diphenylethylene (Sigma Aldrich), α -methylstyrene (Sigma Aldrich), propylene (Sigma Aldrich), LiAlH₄ (Sigma Aldrich). NMR spectra were recorded on Bruker Avance III 300 or Avance III 400 MHz spectrometers and the spectra were calibrated to the residual solvent signals (benzene- d_6 : $\delta_H = 7.16$ ppm, THF- d_8 : $\delta_H = 1.74$ and 3.58 ppm, toluene- d_8 : $\delta_H = 2.08$ ppm). Magnetic moments in solution (benzene- d_6) were determined at room temperature by Evans' method as modified by Sur and corrected for diamagnetic contribution.^[46] LIFDI (Linden CMS) mass spectra were measured by the Zentrale Massenabteilung, Fakultät für Chemie, Georg-August-Universität. Elemental analyses were obtained from the Analytisches Labor, Georg-August-Universität using an Elementar Vario EL 3 analyzer. IR spectra were obtained in Nujol on a Thermo Nicolet iZ10 and using a Bruker ALPHA FTIR spectrometer with Platinum ATR module. Electronic absorption spectra were recorded with a Varian Cary 300 Scan spectrophotometer and an Agilent Cary 60 equipped with an Unisoko Cryostat (CoolSpek) using *J*-Young quartz cuvettes. EPR measurements were performed in air-tight *J*-Young quartz tubes in an atmosphere of purified argon. Frozen solution EPR spectra were recorded on a Bruker EMX-plus CW X-band spectrometer equipped with a Bruker ER 4112HV-CF100 helium cryostat. The spectra were obtained on freshly prepared solutions of 1–10 mM compound and simulated using EasySpin^[47] via the cwEPR GUI.^[48] Temperature-dependent magnetic susceptibility measurement was carried out with a Quantum-Design MPMS3 SQUID magnetometer equipped with a 7 Tesla magnet in the range from 210 to 2.0 K at a magnetic field of 0.5 T.

Synthesis of [CoH(PNP)] (1): A vial was charged with [CoCl(PNP)] (50.0 mg, 0.111 mmol), LiAlH₄ (2.1 mg, 0.055 mmol) and THF (10 mL). The reaction mixture was stirred at room temperature for 1 min. The solvent of the orange solution was removed *in vacuo*. The residue was extracted with pentanes and the resulting solution was filtered over Celite, and dried *in vacuo*. The residue was dissolved in pentanes and recrystallized at -36°C overnight. The solution was decanted and the orange crystalline material (yield: 35 mg, 76%) was dried *in vacuo*. Anal. Found (Calcd) for C₂₀H₄₁CoNP₂: C, 57.28 (57.68); H, 9.89 (9.92); N, 3.36 (3.36). $\mu_{\text{eff}} = 1.97 \pm 0.27$ μ_B . ¹H NMR (C₆D₆, 300 MHz, ppm): 9.85 (tBu), -26.28 (CH₂), -48.28 (CH₂), the hydride signal was not found; ATR-IR: $\tilde{\nu}_{\text{CoH}} = 1756$ cm^{-1} . The isotopologue [CoD(PNP)] (2-D) was analogously prepared from [CoCl(PNP)] (40.0 mg, 0.088 mmol) and LiAlD₄ (1.9 mg, 0.044 mmol) and obtained in as orange crystalline product (yield: 25 mg, 69%). ¹H NMR (C₆D₆, 300 MHz, ppm): 9.63 (tBu), -26.53 (CH₂), -46.97 (CH₂); ATR-IR: $\tilde{\nu}_{\text{CoD}} = 1269$ cm^{-1} .

Synthesis of [Co(PNP)] (2): A vial was charged with [CoCl(PNP)] (50.0 mg, 0.111 mmol), KC₈ (18 mg, 0.133 mmol) and Na/K dried THF (10 mL). The reaction mixture was stirred under static vacuum at room temperature overnight. The solvent of the solution was removed *in vacuo*. ¹H NMR (THF- d_8 , 300 MHz, ppm): 27.35 (tBu), 86.84 (CH), -90.62 (CH).

Synthesis of [CoN₂(PNP)] (3): A vial was charged with [CoCl(PNP)] (50.0 mg, 0.111 mmol), KC₈ (18 mg, 0.133 mmol) and THF (10 mL). The reaction mixture was stirred under N₂ atmosphere at room temperature overnight. The solvent of the solution was removed *in vacuo*. The residue was extracted with pentanes and the resulting solution was filtered, and dried *in vacuo*. The residue was dissolved

in pentanes and recrystallized at -36°C overnight. The solution was decanted and the dark purple crystalline material (yield: 44 mg, 90%) was dried *in vacuo*. Anal. Found (Calcd) for C₂₀H₄₁CoNP₂: C, 54.32 (54.17); H, 9.39 (9.09); N, 9.12 (9.48). ³¹P NMR (C₆D₆, 300 MHz, ppm): 81.6. ¹H NMR (C₆D₆, 300 MHz, ppm): 1.47 (36 H, CH₃, A₁₈BCXX'A'₁₈B'C', ³J_{AX} = 12.97 Hz), 4.01 (2H, PCH, ³J_{BC} = 5.23 Hz), 6.65 (2H, NCH, $N = |^3J_{\text{CX}} + ^3J_{\text{CX}}| = 37.67$ Hz, ³J_{BC} = 5.23 Hz). ATR-IR: $\tilde{\nu}_{\text{NN}} = 2012$ cm^{-1} .}}}

Photolysis of 1 in C₆D₆: 1 (5.0 mg, 0.012 mmol) in 0.4 mL C₆D₆ in a *J*-Young NMR tube was degassed by two freeze-pump-thaw cycles. The solution was photolyzed by a 390 nm LED lamp in a water bath at room temperature. The same procedure was carried out for the photolysis in different deuterated solvents.

Synthesis of [Co(CH₂CH₂Ph)(PNP)] (5): PhCH₂CH₂MgCl (1 M, 0.15 mL, in THF) was dropwise added to the solution of [CoCl(PNP)] (15.0 mg, 0.033 mmol) in THF (4 mL). The reaction mixture was stirred at room temperature for 1 h and the solvent subsequently removed *in vacuo*. The residue was extracted with pentanes. After filtration, the solution was dried *in vacuo*. The residue was dissolved in pentanes and recrystallized at -36°C overnight. The solution was decanted and the dark red crystalline product dried *in vacuo* (yield: 7.8 mg, 45%). Anal. Found (Calcd) for C₂₈H₄₉CoNP₂: C, 64.25 (64.60); H, 9.46 (9.49); N, 2.64 (2.69). ¹H NMR (C₆D₆, 300 MHz, ppm): 13.98 (tBu), 3.85, 0.24, -6.56 , -23.01 , -58.69 , -71.92 .

General procedure for photo-induced olefin hydrogenation: In a typical experiment, complex 1 (2 mg, 4.8 μmol , 1 eq.) and hexamethylbenzene (2 mg, 12.3 μmol , 2.5 eq.) as internal standard were dissolved in C₆D₆ (0.45 mL) in a *J*-Young NMR tube. After addition of the substrate (48 μmol , 10 eq.), the NMR tube was degassed by one freeze-pump-thaw cycle and 1 bar of hydrogen gas was added after warming to room temperature. The resulting solution was then photolyzed at 390 nm (LED), while the temperature was kept at room temperature using a water bath. The conversion and yield were determined by ¹H NMR spectroscopy.

Crystallographic details: Single crystals of 1 and 3 were selected from the mother liquor under an inert gas atmosphere and transferred in protective perfluoro polyether oil on a microscope slide. The selected and mounted crystals were transferred to the cold gas stream on the diffractometer. The diffraction data were obtained at 100 K on a Bruker D8 three-circle diffractometer, equipped with a PHOTON 100 CMOS detector and an INCOATEC microfocus source with Quazar mirror optics (Mo-K α radiation, $\lambda = 0.71073$ Å). The data obtained were integrated with SAINT and a semi-empirical absorption correction from equivalents with SADABS was applied. The structure was solved and refined using the Bruker SHELX 2014 software package.^[49] All non-hydrogen atoms were refined with anisotropic displacement parameters. All C–H hydrogen atoms were refined isotropically on calculated positions by using a riding model with their U_{iso} values constrained to 1.5 U_{eq} of their pivot atoms for terminal sp³ carbon atoms and 1.2 times for all other atoms. The Co–H hydrogen atom in 1 was found from the residual density map and isotropically refined.

Deposition Numbers 2078520 (for 1) and 2078519 (for 3) contain the supplementary crystallographic data for this paper. These data are provided free of charge by the joint Cambridge Crystallographic Data Centre and Fachinformationszentrum Karlsruhe Access Structures service www.ccdc.cam.ac.uk/structures.

Computational details: Density functional theory (DFT) calculations of Gibbs free energies were carried out with the ORCA program package.^[50] Due to charge transfer between the sterically close-lying parts of the tert-butyl groups to the central cobalt atom in 1, the range-separated ω B97X–D3BJ functional^[51] was employed together with the zeroth-order regular approximation (ZORA) for

scalar relativistic effects^[52] and the corresponding ZORA-def2-TZVP basis set.^[53] The resolution of identity and chain of spheres exchange (RIJCOSX) algorithm^[54] with automatically selected auxiliary basis sets^[55] was invoked to speed up the calculations. The Conductor-like Polarizable Continuum Model (CPCM)^[56] was used to model the solvent benzene. In order to avoid numerical instabilities, a Gaussian smearing^[57] was employed for the point charges. The state characters and the electronic absorption spectrum were additionally modelled in ORCA with SC-NEVPT2/CASSCF (strongly contracted *N*-electron valence state perturbation theory on top of complete active space self-consistent field) calculations on a reduced model of **1**, where the *tert*-butyl groups were replaced with methyl groups, employing an active space of 11 electrons in 14 orbitals, a def2-TZVP basis set,^[53] the RI-JK (resolution of identity for Coulomb and exchange integrals) approximation,^[58] and perturbative spin-orbit couplings for 20 quartet and 30 doublet states. EPR spectra of the complex **1** were calculated both with DFT as a single-reference method and SC-NEVPT2 as a multiconfigurational method. The DFT calculations were carried out with the ADF program^[59] using the ω B97X-D functional,^[51] a TZ2P basis set,^[60] ZORA including spin-orbit effects, and toluene as implicit solvent. The SC-NEVPT2 calculations were done as described above, using only 2 quartet and 3 doublet states to save computational time.

Transient spectroscopy: Femtosecond UV-pump/mid-infrared-probe (UV/mIR) and UV-pump/near-UV-to-visible probe (UV/nUV-vis) spectroscopy was carried out with a setup previously described elsewhere.^[61] In brief, 60 fs-duration pulses with a center wavelength of 800 nm were provided by a commercial Ti:sapphire oscillator/regenerative amplifier front-end system (Newport Spectra Physics, Solstice Ace) at a repetition rate of 1 kHz. In both experiments, pump pulses centered at 400 nm were generated by frequency doubling the front-end output in a type-I BBO crystal. MIR-probe pulses tunable between 6 and 8 μ m were generated by difference frequency mixing of the signal and idler pulses of a properly tuned home-built optical parametric amplifier (OPA) in a type-I AgGaS₂ crystal. Vis-to-near-UV white light continuum probe pulses with a spectrum covering the range from 380 nm to 950 nm were generated by focusing a small fraction of the signal pulses of a commercial OPA (tuned to 1240 nm, TOPAS prime, Light Conversion) into a CaF₂-substrate. UV/nUV-vis spectra were recorded with a commercial transient absorption spectrometer (TAS, Newport/Spectra Physics). Solutions of **1** and **1-D** in *n*-hexane, benzene-*h*₆, as well as benzene-*d*₆ were prepared in a glovebox and measured in a sealed stationary sample cell to minimize decomposition upon contact with moisture and air. For the UV/mIR experiments, the sample cell was equipped with two CaF₂ windows that were held apart by a lead spacer at a distance of 100 μ m. Probing in the mid-IR with benzene solutions was not possible due to strong solvent background absorptions in the spectral regions of interest. For the UV/nUV-vis experiment, a commercial cell (Hellma, QS) with an optical pathlength of 1 mm optical path was used. Each measurement was repeated several times with fresh solutions in thoroughly cleaned cuvettes. A slow degradation of the sample over a period of several hours was observed and the dinitrogen complex **3** was found to accumulate in the small sample volume of about 350 μ L.

Acknowledgements

This work was supported by Deutsche Forschungsgemeinschaft (DFG) within Priority Program SPP 2102 "Light-controlled reactivity of metal complexes" (GO1059/8-1, SCHN950/6-1,

VO593/8-1). Open access funding enabled and organized by Projekt DEAL.

Conflict of Interest

The authors declare no conflict of interest.

Keywords: cobalt · hydrogenation · hydrogen atom transfer · photochemistry · transient absorption spectroscopy

- [1] a) *Handbook of Homogeneous Hydrogenation* (Eds.: J. G. de Vries, C. J. Elsevier), Wiley-VCH, Weinheim, **2007**; b) X. Zhang, Y. Chi, W. Tang, in: *Comprehensive Organometallic Chemistry III* (Eds.: D. M. Mingos, R. H. Crabtree), Vol. 10, Elsevier, Amsterdam, **2007**, p. 1–70; c) H. U. Blaser, B. Pugin, F. Spindler, in: *Applied Homogeneous Catalysis with Organometallic Compounds* (Eds.: B. Cornils, W. A. Herrmann, M. Beller, R. Paciello), Wiley-VCH, Weinheim, **2018**, p. 621–644.
- [2] a) P. J. Chirik, *Acc. Chem. Res.* **2015**, *48*, 1687–1695; b) L. Alig, M. Fritz, S. Schneider, *Chem. Rev.* **2019**, *119*, 2681–2751; c) W. Ai, R. Zhong, X. Liu, Q. Liu, *Chem. Rev.* **2019**, *119*, 2876–2953.
- [3] a) Q. Knijnenburg, A. D. Horton, H. van der Heijden, T. M. Kooistra, D. G. H. Hetterscheid, J. M. M. Smits, B. de Bruin, P. H. M. Budzelaar, A. W. Gal, *J. Mol. Catal. A* **2005**, *232*, 151–159; b) G. Zhang, B. L. Scott, S. K. Hanson, *Angew. Chem. Int. Ed.* **2012**, *51*, 12102–12106; *Angew. Chem.* **2012**, *124*, 12268–12272; c) S. Monfette, Z. R. Turner, S. P. Semproni, P. J. Chirik, *J. Am. Chem. Soc.* **2012**, *134*, 4561–4564; d) T.-P. Lin, J. C. Peters, *J. Am. Chem. Soc.* **2013**, *135*, 15310–15313; e) R. P. Yu, J. M. Darmon, C. Milsman, G. W. Margulieux, S. C. E. Stieber, S. DeBeer, P. J. Chirik, *J. Am. Chem. Soc.* **2013**, *135*, 13168–13184; f) D. Gärtner, A. Welther, B. Rezaei, R. Wolf, A. J. von Wangelin, *Angew. Chem. Int. Ed.* **2014**, *53*, 3722–3726; *Angew. Chem.* **2014**, *126*, 3796–3800; g) K. Tokmic, C. R. Markus, L. Zhu, A. R. Fout, *J. Am. Chem. Soc.* **2016**, *138*, 11907–11913; h) J. Chen, C. Chen, C. Ji, Z. Lu, *Org. Lett.* **2016**, *18*, 1594–1597; i) L. S. Merz, C. K. Blasius, H. Wadepohl, L. H. Gade, *Inorg. Chem.* **2019**, *58*, 6102–6113; j) S. Sandl, T. M. Maier, N. P. van Leest, S. Kröncke, U. Chakraborty, S. Demeshko, K. Koszinowski, B. de Bruin, F. Meyer, M. Bodensteiner, C. Herrmann, R. Wolf, A. Jacobi von Wangelin, *ACS Catal.* **2019**, *9*, 7596–7606; k) L. N. Mendelsohn, C. S. MacNeil, L. Tian, Y. Park, G. D. Scholes, P. J. Chirik, *ACS Catal.* **2021**, *11*, 1351–1360; l) H. Alawisi, H. D. Arman, Z. J. Tonzetich, *Organometallics* **2021**, *40*, 1062–1070.
- [4] a) G. Zhang, K. V. Vasudevan, B. L. Scott, S. K. Hanson, *J. Am. Chem. Soc.* **2013**, *135*, 8668–8681; b) Y. Jing, X. Chen, X. Yang, *Organometallics* **2015**, *34*, 5716–5722.
- [5] a) A. Studer, D. P. Curran, *Angew. Chem. Int. Ed.* **2016**, *55*, 58–102; *Angew. Chem.* **2016**, *128*, 58–106; b) E. C. Gentry, R. R. Knowles, *Acc. Chem. Res.* **2016**, *49*, 1546–1556; c) H. Matsubara, T. Kawamoto, T. Fukuyama, I. Ryu, *Acc. Chem. Res.* **2018**, *51*, 2023–2035; d) S. A. Green, S. W. M. Crossley, J. L. M. Matos, S. Vásquez-Céspedes, S. L. Shevick, R. A. Shenvi, *Acc. Chem. Res.* **2018**, *51*, 2628–2640; e) D. Leifert, A. Studer, *Acc. Chem. Res.* **2020**, *53*, 74–108.
- [6] a) D. C. Eisenberg, J. R. Norton, *Isr. J. Chem.* **1991**, *31*, 55–66; b) B. de Bruin, W. I. Dzik, S. Li, B. B. Wayland, *Chem. Eur. J.* **2009**, *15*, 4312–4320.
- [7] S. W. M. Crossley, C. Obradors, R. M. Martinez, R. A. Shenvi, *Chem. Rev.* **2016**, *116*, 8912–9000.
- [8] Representative Examples: a) J. Choi, L. Tang, J. R. Norton, *J. Am. Chem. Soc.* **2007**, *129*, 234–240; b) J. Hartung, M. E. Pulling, D. M. Smith, D. X. Yang, J. R. Norton, *Tetrahedron* **2008**, *64*, 11822–11830; c) S. W. Crossley, F. Barabé, R. A. Shenvi, *J. Am. Chem. Soc.* **2014**, *136*, 16788–16791; d) J. L. Kuo, J. Hartung, A. Han, J. R. Norton, *J. Am. Chem. Soc.* **2015**, *137*, 1036–1039; e) G. Li, J. L. Kuo, A. Han, J. M. Abuyuan, L. C. Young, J. R. Norton, J. H. Palmer, *J. Am. Chem. Soc.* **2016**, *138*, 7698–7704; f) K. Iwasaki, K. K. Wan, A. Oppedisano, S. W. M. Crossley, R. A. Shenvi, *J. Am. Chem. Soc.* **2014**, *136*, 1300–1303; g) C. Obradors, R. M. Martinez, R. A. Shenvi, *J. Am. Chem. Soc.* **2016**, *138*, 4962–4971.
- [9] S. L. Shevick, C. V. Wilson, S. Kotesova, D. Kim, P. L. Holland, R. A. Shenvi, *Chem. Sci.* **2020**, *11*, 12401–12422.
- [10] M. R. Schreier, B. Pfund, X. Guo, O. S. Wenger, *Chem. Sci.* **2020**, *11*, 8582–8594.

- [11] a) M. Tilset, V. D. Parker, *J. Am. Chem. Soc.* **1989**, *111*, 6711–6717; b) G. Kiss, K. Zhang, S. L. Mukerjee, C. D. Hoff, G. C. Roper, *J. Am. Chem. Soc.* **1990**, *112*, 5657–5658.
- [12] Y.-R. Luo, *Comprehensive Handbook of Chemical Bond Energies*, CRC Press, Boca Raton, 1st Edition, **2007**.
- [13] The solution $BDFE_{C-H}$ of hydrocarbons in toluene were estimated from the reported gas phase $BDFE_{C-H}$ using: $BDFE_{C-H}^{sol} \approx BDFE_{C-H}^{gas} - 3.4 \text{ kcal} \cdot \text{mol}^{-1}$. For details see the Electronic Supporting Information and Ref. [14].
- [14] J. J. Warren, T. A. Tronic, J. M. Mayer, *Chem. Rev.* **2010**, *110*, 6961–7001.
- [15] C. F. Wise, R. G. Agarwal, J. M. Mayer, *J. Am. Chem. Soc.* **2020**, *142*, 10681–10691.
- [16] J. Choi, Y. Lee, *Angew. Chem. Int. Ed.* **2019**, *58*, 6938–6942; *Angew. Chem.* **2014**, *131*, 7012–7016.
- [17] P. O. Lagaditis, B. Schluschaß, S. Demeshko, C. Würtele, S. Schneider, *Inorg. Chem.* **2016**, *55*, 4529–4536.
- [18] a) S. P. Semproni, C. Millsman, P. J. Chirik, *J. Am. Chem. Soc.* **2014**, *136*, 9211–9224; b) S. Kuriyama, K. Arashiba, H. Tanaka, Y. Matsuo, K. Nakajima, K. Yoshizawa, Y. Nishibayashi, *Angew. Chem.* **2016**, *55*, 14291–14295; c) L. M. Guard, T. J. Hebden, D. E. Linn, Jr., D. M. Heinekey, *Organometallics* **2017**, *36*, 3104–3109.
- [19] R. H. Morris, *Inorg. Chem.* **2018**, *57*, 13809–13821.
- [20] Y. Nishida, S. Kida, *Coord. Chem. Rev.* **1979**, *27*, 275–298.
- [21] a) Y. Nishida, A. Sumita, S. Kida, *Bull. Chem. Soc. Jpn.* **1977**, *50*, 759–760; b) Y. Nishida, K. Hayashi, A. Sumita, S. Kida, *Bull. Chem. Soc. Jpn.* **1980**, *53*, 271–272; c) Z. Mo, Y. Li, L. Deng, *Organometallics* **2011**, *30*, 4687–4694; d) J. A. Przyojski, H. D. Arman, Z. J. Tonzetich, *Organometallics* **2013**, *32*, 723–732; e) M. R. Friedfeld, G. W. Margulieux, B. A. Schaefer, P. J. Chirik, *J. Am. Chem. Soc.* **2014**, *136*, 13178–13181.
- [22] a) R. R. Horn, G. W. Everett, Jr., *J. Am. Chem. Soc.* **1971**, *93*, 7173–7178; b) B. Evans, K. N. Smith, G. N. La Mar, D. B. Viscio, *J. Am. Chem. Soc.* **1977**, *99*, 7070–7072; c) N. Hebenandaz, F. H. Köhler, F. Scherbaum, B. Schlesienger, *Magn. Reson. Chem.* **1989**, *27*, 798–802; d) K. H. Theopold, J. Silvestre, E. K. Byrne, D. S. Richeson, *Organometallics* **1989**, *8*, 2001–2009; e) C. J. Medforth, F.-Y. Shiau, G. N. La Mar, K. M. Smith, *J. Chem. Soc., Chem. Commun.* **1991**, 590–592; f) R. A. Heintz, T. G. Neiss, K. H. Theopold, *Angew. Chem. Int. Ed. Engl.* **1994**, *33*, 2326–2328; g) N. L. Wieder, M. Gallagher, P. J. Carroll, D. H. Berry, *J. Am. Chem. Soc.* **2010**, *132*, 4107–4109; h) R. Beck, M. Shoshani, S. A. Johnson, *Angew. Chem. Int. Ed.* **2012**, *51*, 11753–11756; *Angew. Chem.* **2012**, *124*, 11923–11926; i) T. R. Dugan, E. Bill, K. C. MacLeod, W. W. Brennessel, P. L. Holland, *Inorg. Chem.* **2014**, *53*, 2370–2380.
- [23] a) I. Bertini, C. Luchinat, *Coord. Chem. Rev.* **1996**, *150*, 29–75. b) B. Martin, J. Autschbach, *J. Chem. Phys.* **2017**, *142*, 054108.
- [24] R. P. Yu, J. M. Darmon, C. Millsman, G. W. Margulieux, S. C. Stieber, S. DeBeer, P. J. Chirik, *J. Am. Chem. Soc.* **2013**, *135*, 13168–13184.
- [25] a) M. Ingleson, H. Fan, M. Pink, J. Tomaszewski, K. G. Caulton, *J. Am. Chem. Soc.* **2006**, *128*, 1804–1805; b) T. Suzuki, K. Fujimoto, Y. Takemoto, Y. Wasada-Tsutsui, T. Ozawa, T. Inomata, M. D. Fryzuk, H. Masuda, *ACS Catal.* **2018**, *8*, 3011–3015.
- [26] S. J. Connelly, Robison, D. M. Heinekey, *Chem. Commun.* **2017**, *53*, 669–676.
- [27] a) C. Bianchini, C. Mealli, M. Peruzzini, F. Zenobi *J. Am. Chem. Soc.* **1992**, *114*, 5905–5906; b) D. M. Heinekey, A. Liegeois, M. v. Roon, *J. Am. Chem. Soc.* **1994**, *116*, 8388–8389; c) T. J. Hebden, J. A. St. John, D. G. Gusev, V. Kaminsky, K. I. Goldberg, D. M. Heinekey, *Angew. Chem. Int. Ed.* **2011**, *50*, 1873–1876; *Angew. Chem.* **2011**, *123*, 1913–1916; d) W. E. Gundersen, D. L. M. Suess, H. Fong, X. Wang, C. M. Hoffmann, G. E. Cutsail III, J. C. Peters, B. M. Hoffman, *J. Am. Chem. Soc.* **2014**, *136*, 14998–15009; e) K. Tokmic, A. R. Fout, *J. Am. Chem. Soc.* **2016**, *138*, 13700–13705; f) M. V. Vollmer, J. Xie, C. C. Lu, *J. Am. Chem. Soc.* **2017**, *139*, 6570–6573; g) M. M. Deegan, K. I. Hannoun, J. C. Peters, *Angew. Chem. Int. Ed.* **2020**, *59*, 22631–22637; *Angew. Chem.* **2020**, *132*, 22820–22826.
- [28] The term $BDFE_{C-H2}$ is used for the free energy that is required to remove a hydrogen atom, irrespective whether it is a dihydride or dihydrogen complex.
- [29] a) J. Halpern, M. Pribanic, *Inorg. Chem.* **1970**, *9*, 2616–2618; b) B. B. Wayland, S. A. E. Sherry, *Inorg. Chem.* **1992**, *31*, 148–150; c) K. B. Capps, A. Bauer, G. Kiss, C. D. Hoff, *J. Organomet. Chem.* **1999**, *586*, 23–30; d) J. R. Norton, T. Spataru, D. Camaoni, S.-J. Lee, G. Li, J. Choi, J. A. Franz, *Organometallics* **2014**, *33*, 2496–2502; e) G. Li, D. P. Estes, J. R. Norton, S. Ruccolo, A. Sattler, W. Sattler, *Inorg. Chem.* **2014**, *53*, 10743–10747.
- [30] C. D. Hoff, *Coord. Chem. Rev.* **2000**, *206–207*, 451–467.
- [31] R. N. Perutz, B. Procacci, *Chem. Rev.* **2016**, *116*, 8506–8544.
- [32] Photolysis of **1** in C_6D_6 under argon gave, besides **1-D**, the N_2 complex **3** as side product (~20%), which is attributed to the presence of trace amounts of dinitrogen. Accordingly, photolysis of **1** under N_2 (1 bar, 12 selectively gives **3**.
- [33] R. L. Sweany, in *Transition metal hydrides* (Ed.: A. Dedieu) VCH: New York, **1992**, p. 65–101.
- [34] a) A. Veillard, A. Strich, *J. Am. Chem. Soc.* **1988**, *110*, 3793–3797; b) C. Daniel, *J. Am. Chem. Soc.* **1992**, *114*, 1625–1631; c) M. C. Heitz, D. Guillaumont, I. Cote-Bruand, C. Daniel, *J. Organomet. Chem.* **2000**, *609*, 66–76; d) D. Ambrosek, S. Villaume, C. Daniel, L. González, *J. Phys. Chem. A* **2007**, *111*, 4737–4742.
- [35] a) R. Ziesel, *Angew. Chem. Int. Ed. Engl.* **1991**, *30*, 844–847; *Angew. Chem.* **1991**, *103*, 863–866; *Angew. Chem. Int. Ed.* **1991**, *30*, 844–847; b) R. Ziesel, *J. Am. Chem. Soc.* **1993**, *115*, 118–127; c) C. L. Pitman, A. J. M. Miller, *ACS Catal.* **2014**, *4*, 2727–2733; d) S. M. Barrett, B. M. Stratakes, M. B. Chambers, D. A. Kurtz, C. L. Pitman, J. L. Dempsey, A. J. M. Miller, *Chem. Sci.* **2020**, *11*, 6442–6449.
- [36] T. Suenobu, D. M. Guldi, S. Ogo, S. Fukuzumi, *Angew. Chem. Int. Ed.* **2003**, *42*, 5492–5495; *Angew. Chem.* **2003**, *115*, 5650–5653.
- [37] a) S. M. Barrett, C. L. Pitman, A. G. Walden, A. J. M. Miller, *J. Am. Chem. Soc.* **2014**, *136*, 14718–14721; b) M. B. Chambers, D. A. Kurtz, C. L. Pitman, M. K. Brennaman, A. J. M. Miller, *J. Am. Chem. Soc.* **2016**, *138*, 13509–13512.
- [38] F. Schneck, J. Ahrens, M. Finger, A. C. Stückl, C. Würtele, D. Schwarzer, S. Schneider, *Nat. Commun.* **2018**, *9*, 1–8.
- [39] C. M. Taliaferro, E. O. Danilov, F. N. Castellano, *J. Phys. Chem. A* **2018**, *122*, 4430–4436.
- [40] B. Wezislá, J. Lindner, U. Das, A. C. Filippou, P. Vöhringer, *Angew. Chem. Int. Ed.* **2017**, *56*, 6901–6905; *Angew. Chem.* **2017**, *129*, 7005–7009.
- [41] R. M. Bullock, E. G. Samsel, *J. Am. Chem. Soc.* **1990**, *112*, 6886–6898.
- [42] D. J. Goebbert, P. G. Wenthold, *Int. J. Mass Spectrometry* **2006**, *257*, 1–11.
- [43] D. F. McMillen, D. M. Golden, *Ann. Rev. Phys. Chem.* **1982**, *33*, 493–532.
- [44] a) S. S. Rozenel, R. Padilla, C. Camp, J. Arnold, *Chem. Commun.* **2014**, *50*, 2612–2614; b) A. R. Fout, F. Basuli, H. Fan, J. Tomaszewski, J. C. Huffman, M.-H. Baik, D. J. Mendiola, *Angew. Chem. Int. Ed.* **2006**, *45*, 3291–3295; *Angew. Chem.* **2006**, *118*, 3369–3373.
- [45] S. Engl, O. Reiser, *ACS Catal.* **2020**, *10*, 9899–9906
- [46] a) D. F. Evans, *J. Chem. Soc.* **1959**, 2003; b) S. K. Sur, *J. Magn. Reson.* **1989**, *82*, 169–173.
- [47] EasySpin, a comprehensive software package for spectral simulation and analysis in EPR. S. Stoll, A. Schweiger *J. Magn. Reson.* **2006**, *178*, 42–55.
- [48] Thomas Casey (2021). cwEPR (<https://www.mathworks.com/matlabcentral/fileexchange/73292-cwepwr>), MATLAB Central File Exchange.
- [49] a) APEX3 v2016.9-0 (SAINT/SADABS/SHELXT/SHELXL), Bruker AXS Inc., Madison, WI, USA, 2016; b) G. M. Sheldrick, *Acta Crystallogr.* **2015**, *A71*, 3–8; c) G. M. Sheldrick, *Acta Crystallogr. Sect. C* **2015**, *71*, 3–8; d) G. M. Sheldrick, *Acta Crystallogr.* **2008**, *A64*, 112–122.
- [50] F. Neese, F. Wennmohs, U. Becker, C. Riplinger, *J. Chem. Phys.* **2020**, *152*, 224108.
- [51] Y. Lin, G. Li, S. Mao, J. Chai, *J. Chem. Theory Comput.* **2013**, *9*, 263–272.
- [52] E. van Lenthe, J. G. Snijders, E. J. Baerends, *J. Chem. Phys.* **1996**, *105*, 6505–6516.
- [53] F. Weigend, R. Ahlrichs, *Phys. Chem. Chem. Phys.* **2005**, *7*, 3297–3305.
- [54] F. Neese, F. Wennmohs, A. Hansen, U. Becker, *Chem. Phys.* **2009**, *356*, 98–109.
- [55] G. L. Stoychev, A. A. Auer, F. Neese, *J. Chem. Theory Comput.* **2017**, *13*, 554–562.
- [56] V. Barone, M. Cossi, *J. Phys. Chem. A* **1998**, *102*, 1995–2001.
- [57] D. M. York, M. Karplus, *J. Phys. Chem. A* **1999**, *103*, 11060–11079.
- [58] F. Neese, *J. Comput. Chem.* **2003**, *24*, 1740–1747.
- [59] G. Te Velde, F. M. Bickelhaupt, E. J. Baerends, C. Fonseca Guerra, S. J. A. van Gisbergen, J. G. Snijders, T. Ziegler, *J. Comput. Chem.* **2001**, *22*, 931–967.
- [60] E. Van Lenthe, E. J. Baerends, *J. Comput. Chem.* **2002**, *24*, 1142–1156.
- [61] S. Straub, L. L. Domenianni, J. Lindner, P. Vöhringer, *J. Phys. Chem. B* **2019**, *123*, 7893–7904.

Manuscript received: May 13, 2021
Accepted manuscript online: June 22, 2021
Version of record online: July 20, 2021